Origin of hole density pinning in group-V doped CdTe

Baoying Dou [1,2], Xuefen Cai [3,*] and Su-Huai Wei [1,†]

[1] *Beijing Computational Science Research Center, Beijing 100193, China*
[2] *Henan Key Laboratory of Quantum Materials and Quantum Energy, School of Future Technology, Henan University, Zhengzhou 450046, China*
[3] *College of Physics and Optoelectronic Engineering, Shenzhen University, Shenzhen 518060, China*

(Received 31 July 2023; revised 18 February 2024; accepted 1 May 2024; published 20 May 2024)

Hole densities in group-V (P, As, and Sb) doped CdTe typically fall below 10^{17}cm^{-3} although sufficient group-V dopants are incorporated. Previous theoretical studies suggested that the formation of *AX* centers compensates the acceptors, thereby limiting *p*-type doping. However, recent calculations including spin-orbit coupling effects suggest that *AX* centers are unstable and thus cannot hinder *p*-type doping. Therefore, the origin of the hole density pinning issue in CdTe remains elusive. Our first-principles calculations, incorporating spin-orbit coupling, coupled with detailed balance simulations, reveal that hole doping in CdTe remains significantly limited despite the instability of the *AX* centers. This limitation stems from the self-compensation driven by the native vacancies and the band-edge excitations induced by free carriers. Additionally, we find that As is the most favorable dopant among group-V dopants due to its relatively low formation energy and shallow transition level. Our understanding of the hole-limiting mechanism is important for improving the dopability of CdTe solar cells. Moreover, our analysis of the band-edge excitations is critical for describing the defect properties in semiconductors.

DOI: 10.1103/PhysRevB.109.205205

I. INTRODUCTION

CdTe has a large optical absorption coefficient and an appropriate band gap of around 1.5 eV which matches well with the solar spectrum [1–3], making it an attractive absorber material for efficient thin-film solar cells. CdTe thin-film solar cells are competitive in commercial applications due to their low fabrication cost and improved efficiency. The recorded efficiency has achieved 22.6% [4], but still falls short of the maximum theoretical efficiency of around 32%. This discrepancy is primarily attributed to the low open circuit voltage (V_{oc}) [5,6], which results from the low hole density. A typical CdTe film is doped under Cd-poor conditions to produce V_{Cd} or Cu_{Cd}, but the Cd-poor conditions often lead to the formation of recombination centers such as Te antisites and Te interstitials [7,8]. Additionally, the hole density is low in the range of $10^{14}-10^{15}$cm^{-3} [6,9,10]. Doping CdTe with group-V (P, As, and Sb) elements under Cd-rich conditions has emerged as a promising approach, which has shown potential in increasing the hole density to $>10^{16}$cm^{-3} [11–13]. However, a perplexing observation persists: the hole density in group-V doped CdTe remains pinned below 10^{17}cm^{-3}, despite the sufficient incorporation of group-V dopants [11–15].

To elucidate the doping limit in group-V doped CdTe, previous theoretical calculations [9,16–18] suggested that the formation of *AX* centers, acting as positively charged deep donors, compensates the acceptors and thus limits the doping process. Recent first-principles studies [19–22] highlighted the significant impact of spin-orbit coupling (SOC) on defect properties, particularly when heavy atoms such as Pb and Te are involved. In PbTe [23], for instance, SOC narrows the band gap and greatly alters the positions of band edges, resulting in the prediction of native *n*-type behavior instead of the native *p*-type in the absence of SOC. In the context of CdTe, it has been reported that SOC effects have more influence on the localized acceptor states formed by Te *p* orbitals, and the transition levels are determined by the combined movement of band edges and defect states [24]. Most importantly, it is proposed that with the inclusion of SOC, *AX* centers become unstable, thus challenging their role in limiting *p*-type doping [25]. Therefore, the underlying mechanism responsible for the doping limits in group-V doped CdTe remains elusive.

In this paper, we conduct a comprehensive investigation in group-V doped CdTe using a hybrid functional, considering the intricate interplay of SOC effects. Firstly, consistent with Ref. [25], we find that the *AX* centers are indeed unstable as they have larger formation energies compared to the desired acceptors. Consequently, *AX* centers appear not to be the origin of the hole doping limit. Secondly, through a systematic numerical study of the detailed balance equations, we identify that the thermal band-edge excitations and native vacancies strongly compensate for *p*-type doping in CdTe. Additionally, we find that all group-V dopings achieve hole densities within the range of $10^{15}-10^{17}$cm^{-3}. Arsenic doping emerges as the most effective, with the highest hole density of $\sim10^{17}$cm^{-3} among group-V doping, attributed to its relatively low formation energy and shallow acceptor level. Our findings provide valuable insights into the doping limits of CdTe and

*caixuefen@szu.edu.cn
†suhuaiwei@csrc.ac.cn

 ©2024 American Physical Society

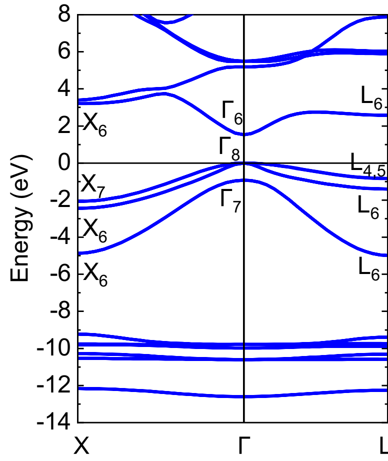

FIG. 1. Calculated band structure of CdTe.

offer guidance for experimental synthesis. The understanding of band-edge excitations presented in this study is important and holds a key role in understanding the doping behavior of narrow band gap semiconductors.

II. COMPUTATIONAL METHODS

Our first-principles calculations are conducted using density functional theory (DFT) with the projector augmented wave (PAW) method [26], as implemented in the Vienna *ab initio* simulation package (VASP) [27]. The Heyd-Scuseria-Ernzerhof 2006 (HSE06) hybrid functional [28] ($\alpha = 0.33$) including spin-orbit coupling [29] is adopted to obtain a band gap of 1.52 eV and a lattice constant of 6.55 Å for bulk CdTe, in good agreement with the experimental results of 1.56 eV and 6.48 Å [30], respectively. As shown in Fig. 1, CdTe is a direct band gap semiconductor, with the conduction band minimum (CBM) and the valence band maximum (VBM) both located at the Γ point. The valence band at the Γ point is split into degenerate heavy-hole and light-hole states (Γ_8), and a spin-orbit split-off state (Γ_7). Plane-wave functions are expanded with a cutoff energy of 350 eV. For defect calculations, we construct a 216-atom supercell ($3 \times 3 \times 3$ of the eight-atom unit cell) and sample the Brillouin zone using a single Γ point. To ensure the convergence of our results, we also employ a larger 512-atom supercell ($4 \times 4 \times 4$ of the eight-atom unit cell) to test the size dependency. All atoms in the supercells are allowed to relax until the forces on each of them become less than 0.01 eV/Å.

To determine the defect formation energy $\Delta H_f(\alpha, q)$, we need to calculate the total energy $E(\alpha, q)$ of a supercell containing the defect α in charge state q, as well as the total energy $E(\text{host})$ of the host without the defect. $\Delta H_f(\alpha, q)$ is a function of the electron Fermi energy E_F (referenced to the VBM) and the atomic chemical potentials μ_i, defined as follows [31]:

$$\Delta H_f(\alpha, q) = \Delta E(\alpha, q) + \sum_i n_i\mu_i + qE_F + E_{\text{corr}}, \quad (1)$$

where $\Delta E(\alpha, q) = E(\alpha, q) - E(\text{host}) + \sum_i n_iE_i + qE_{\text{VBM}}$. n_i represents the number of atoms i transferred from the supercell to the reservoirs of element i in forming the defect. μ_i denotes the chemical potential of atom i, which is referenced to the energy E_i of the elemental solid or gas. The correction term E_{corr} is obtained by aligning the deep $1s$ core levels of the atoms far away from the defect in the supercell with that in the defect-free cell. The defect transition energy level is the Fermi energy E_F, where the formation energies of defect α in charge states q and q' are equivalent, i.e.,

$$\epsilon_\alpha(q/q') = [\Delta E(\alpha, q) - \Delta E(\alpha, q')]/(q' - q). \quad (2)$$

Thus, Eq. (1) can be rewritten as

$$\Delta H_f(\alpha, q) = \Delta H_f(\alpha, 0) - q\varepsilon_\alpha(0/q) + qE_F. \quad (3)$$

At a given temperature T, the density n_D^+ of the donor defect with a formation energy of $\Delta H_f(D^+)$, and the density n_A^- of the acceptor defect with a formation energy of $\Delta H_f(A^-)$, conform to the Boltzmann distribution,

$$n_D^+ = N_{\text{site}}g_D e^{-\Delta H_f(D^+)/k_BT},$$
$$n_A^- = N_{\text{site}}g_A e^{-\Delta H_f(A^-)/k_BT}, \quad (4)$$

where N_{site} is the number of available sites for the defect α per unit volume, and g_D and g_A are the degeneracy factors for donors and acceptors, which represent the numbers of possible electron configurations per site.

The concentrations of electrons and holes are determined by [32]

$$p_0 = N_v e^{(E_v - E_F)/k_BT},$$
$$n_0 = N_c e^{-(E_c - E_F)/k_BT}, \quad (5)$$

where E_v and E_c are the VBM and CBM energies, respectively. For convenience, we typically set $E_v = 0$ and $E_c = E_g$, where E_g corresponds to the band gap. Then Eq. (5) can be rewritten as follows:

$$p_0 = N_v e^{-E_F/k_BT},$$
$$n_0 = N_c e^{(E_F - E_g)/k_BT}. \quad (6)$$

Under the parabolic approximation, the effective density of states for the valence band N_v and conduction band N_c are expressed by

$$N_v = 2(2\pi m_{dv}^* k_BT)^{\frac{3}{2}}/h^3,$$
$$N_c = 2(2\pi m_{dc}^* k_BT)^{\frac{3}{2}}/h^3. \quad (7)$$

The density of states effective masses for the valence band and conduction band are given by $m_{dv}^* = \{m_{lh}^{*\,3/2} + m_{hh}^{*\,3/2} + [m_{so}^*\exp(-\Delta/kT)]^{3/2}\}^{2/3}$ and $m_{dc}^* = m_e^*$, respectively, taking into account the spin degeneracy and spin-orbit coupling [33]. Here, m_e^*, m_{lh}^*, m_{hh}^*, and m_{so}^* are the effective masses of electron, light hole, heavy hole, and split-off hole band, respectively, and Δ is the spin-orbit split-off energy. In the calculations, the experimental values of effective masses in CdTe, $m_{dv}^* = 0.84m_0$ and $m_{dc}^* = 0.095m_0$ (m_0 denotes the mass of a free electron), are adopted [34] because the effective masses calculated by different methods often differ from each other [35,36]. Importantly, the difference between calculated and experimental data does not

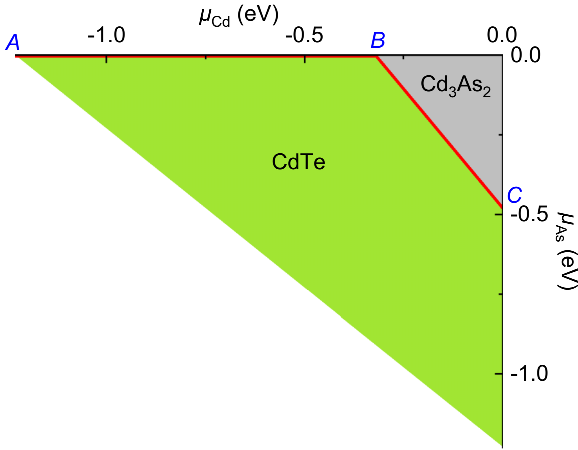

FIG. 2. Chemical-potential stability diagram for As doping in CdTe under equilibrium growth conditions. Within the green region, CdTe is thermodynamically stable, while in the gray region, the competing secondary compounds Cd_3As_2 will form.

impact the magnitude order of the calculated carrier densities. The concentrations of positively charged defect n_D^+ and negatively charged defect n_A^- should satisfy the neutralization condition:

$$p_0 + n_D^+ = n_0 + n_A^-. \quad (8)$$

By solving the equations self-consistently, we can obtain the Fermi energy, carrier densities, and defect concentrations as functions of the chemical potentials at a specific temperature under thermal equilibrium growth conditions.

When the system is quenched from a high growth temperature to room temperature (working temperature), the total concentration of defect α in all possible charge states remains fixed at the value of growth temperature, which is known as "freezing-in" approximation [37]. During this quenching process, the densities of different charged defects will be redistributed according to their respective weights. By utilizing this method, the system can attain a relatively low Fermi energy and high carrier densities.

III. RESULTS AND DISCUSSIONS

Defect formation energy depends strongly on the atomic chemical potential and electronic Fermi level, as seen in Eq. (1). Therefore, the first step in calculating defect properties is to determine the chemical-potential stability diagram. For group-V doping in CdTe, the chemical-potential conditions are $\mu_{Cd} + \mu_{Te} = \Delta H(\text{CdTe})$ and $m\mu_{Cd} + n\mu_X \leqslant \Delta H_f(\text{Cd}_m X_n)$. The calculated $\Delta H(\text{CdTe})$ is -1.23 eV, in good agreement with the experimental value of -1.17 eV [38]. Cd_3P_2, Cd_3As_2, and Cd_3Sb_2 are the competing secondary phases, with the calculated formation energies of -0.57, -0.95, and -0.64 eV, respectively. Taking As doping as an example, as shown in Fig. 2, CdTe is thermally stable within the green region bounded by the red line *A*-*B*-*C*. Points *A*, *B*, and *C* represent Cd-poor/Te-rich/As-rich, Cd-poor/Te-poor/As-rich, and Cd-rich/Te-poor/As-poor conditions, respectively. Along line *A*-*B*, the chemical potentials of Cd and As satisfy $-1.23 < \mu_{Cd} < -0.32$, $\mu_{As} = 0$; along line *B*-*C*, they satisfy $-0.32 < \mu_{Cd} < 0$, $\mu_{As} = -(0.96 + 3\mu_{Cd})/2$. We will discuss the defect properties along the chemical-potential line *A*-*B*-*C* in the following.

For group-V doping in CdTe, group-V dopants prefer to substitute at the Te sites, forming X_{Te} (X = P, As, Sb) defects. Main native defects such as Cd vacancy (V_{Cd}) and Te vacancy (V_{Te}) are also included in our defect calculations. Figure 3(a) shows the dependence of formation energies of these defects in neutral charge states on μ_{Cd}. As μ_{Cd} increases, the formation energy of V_{Cd} increases linearly while the formation energy of V_{Te} decreases linearly, which can be easily understood from Eq. (1). For X_{Te} (X = P, As, Sb) defects, their formation energies decrease along line *A*-*B*, and then increase along line *B*-*C*, because the chemical potential of group-V dopants obeys different constraints along lines *A*-*B* and *B*-*C* as seen in Fig. 2. We note that the formation energies of P_{Te}, As_{Te}, and Sb_{Te} gradually decrease under identical chemical-potential growth conditions because the size mismatch between group-V atoms and Te is reduced with increasing atomic number. Our calculated formation energies of group-V substitutional defects under Cd-rich and Te-rich conditions are in good agreement with previous calculations [15,18,39].

Figures 3(b)–3(f) show the calculated defect formation energies in group-V doped CdTe as functions of the Fermi level under different chemical-potential growth conditions, i.e., points *A*, *B*, and *C*. The calculated (0/−) transition energy levels for P_{Te}, As_{Te}, and Sb_{Te} are at 0.07, 0.08, and 0.20 eV above the VBM, respectively. The experimental values for P_{Te} and As_{Te} are within the ranges of 35–87 meV [11,41–44] and 55−94 meV [11,45–47], respectively, close to our calculated results. The transition energy level of Sb_{Te} is under debate both experimentally and theoretically. Previous experimental and theoretical studies predicted Sb_{Te} to be a deep acceptor with a deep transition level at 230 meV [9,15,48]. However, in a recent experiment, a shallow level of 103 meV was reported [11], and a recent calculation found it to be 116 meV [25]. We note that the trend in our calculated transition levels aligns with previous calculations [9,15,39], and the absolute values do not affect our conclusions. The increasing deeper defect levels from P to As to Sb can be explained by the fact that the defect states mainly originate from the anion *p* states. As the atom number increases from P to As to Sb, their valence *p* orbital energy rises, resulting in a deeper acceptor level.

The relatively low hole density in group-V doped CdTe has long been attributed to the *AX* center, which compensates acceptors. When forming the *AX* center, the group-V impurity moves towards its nearest neighbor Te along the [110] direction, forming a bond with the Te atom, while breaking their two bonds with Cd. In this case, the threefold degenerate t_2 state will split into a fully occupied doubly degenerated e state and an empty single a_2 state, leading to a gain in electronic energy against the energy cost incurred by breaking the bonds. If the *AX* center stabilizes, it will act as a positively charged deep donor [9,18,39]. Figures 3(b)–3(f) reveal that the *AX* centers for the three group-V dopants all have quite high formation energies. As a result, the (0/+) transition energy levels for the group-V substitutional defect are located within the valence bands. Our results indicate that *AX* centers are not stable, consistent with a recent calculation including SOC [25].

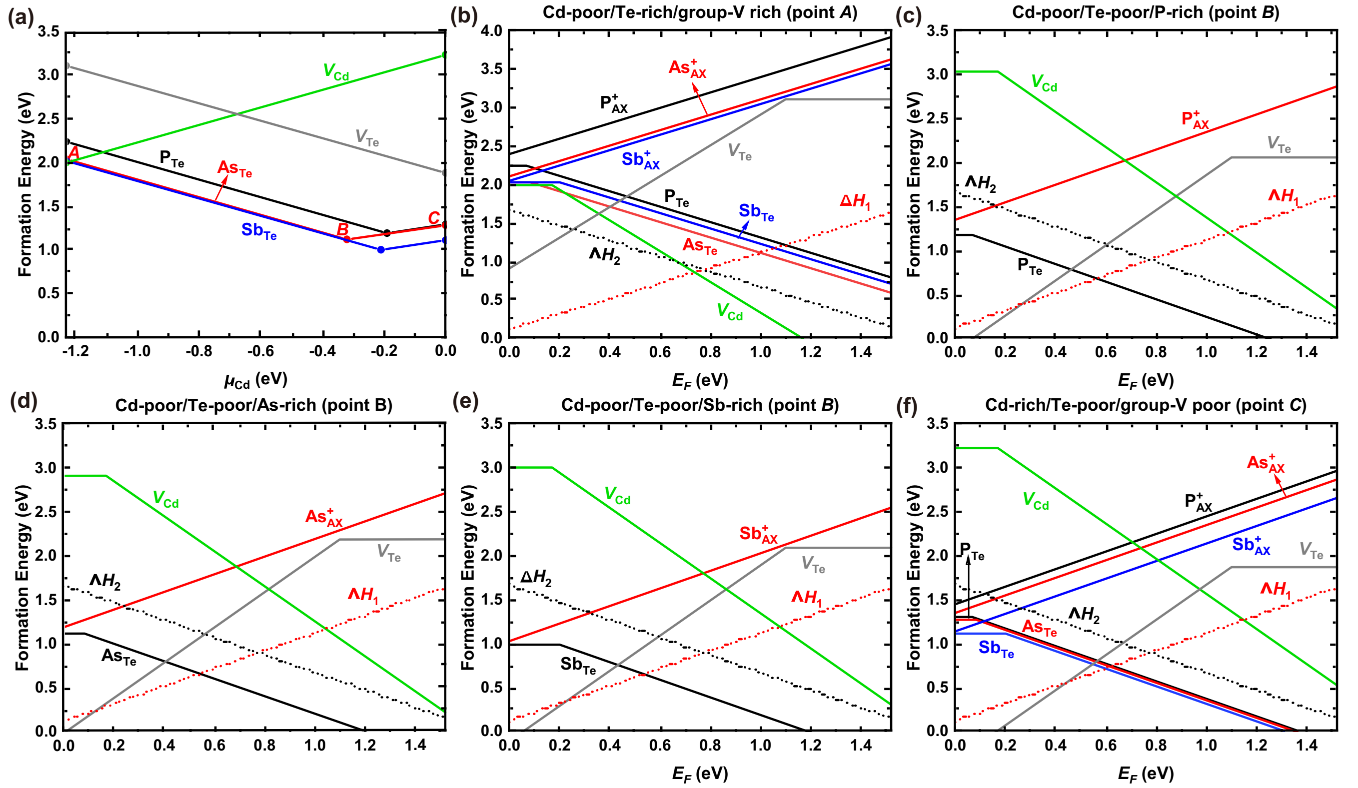

FIG. 3. (a) Calculated formation energies of neutral defects in group-V doped CdTe, as functions of the Cd chemical potential (μ_{Cd}). (b)–(f) Calculated defect formation energies, as functions of the Fermi level (E_F) under different chemical-potential growth conditions. Points A, B, and C represent Cd-poor/Te-rich/group-V rich, Cd-poor/Te-poor/group-V rich, and Cd-rich/Te-poor/group-V poor conditions, respectively. Red and black dashed lines denote host electronic states ΔH_1 and ΔH_2 involved in band-edge excitations. See Ref. [40] for more calculation details about band-edge excitations.

According to prior first-principles calculations [6,24,49,50], V_{Cd}, V_{Te}, and Cd interstitial (Cd_i) are the primary native defects in CdTe. Cd_i is not considered as a limiting factor because of its high formation energy. Our calculations show that charge-neutral V_{Cd} and V_{Te} are the most stable intrinsic defects when accompanied by Jahn-Teller distortion. V_{Cd} has a (0/2−) transition energy level at 0.17 eV above the VBM, and V_{Te} has a (0/2+) transition energy level at 0.42 eV below the CBM. These results are close to previous calculations in Refs. [9,50–52] but different from the results in Refs. [6,24] that found V_{Te} to be a rather shallow donor. For intuitive observations, the band-edge excitations induced by free carriers are incorporated into the defect formation energy vs Fermi energy plot, as shown in the dashed lines in Figs. 3(b)–3(f). In Fig. 3(b), we can see that the negatively charged V_{Cd} and the host electronic state ΔH_1 pin the Fermi level around the middle of the band gap under the chemical potential of point A. In Figs. 3(c)–3(f), both ΔH_1 and V_{Te} compensate the negatively charged defect X_{Te} (X = P, As, Sb), thereby limiting the hole density.

After calculating the defect formation energies, we can determine the Fermi level, carrier densities, and defect concentrations by solving the detailed balance equations (4)–(8) in Sec. II A. CdTe samples are usually grown at high temperatures (e.g., 850 K) and then quenched to room temperature (300 K). The simulations of growth temperature at 300 and 850 K, and quenching from 850 to 300 K are carried out, as shown in Figs. 4–6. We take As doping as an example to analyze the results. One can easily extend to P doping and Sb doping. At $T = 850$ K, as μ_{Cd} increases along the A-B-C line, the Fermi level increases to the highest, then drops to the lowest at point B, and finally increases from point B to point C. This can be understood from Figs. 3(b)–3(f). At the chemical potential of point A, the dominant defects are V_{Cd} and ΔH_1, which pin the Fermi level around the middle of the band gap [Fig. 3(b)]. As μ_{Cd} increases, the formation energy of V_{Cd} gradually rises [Fig. 3(a)], while the formation energies of host electronic states are independent of atomic chemical potentials; consequently, the pinning position of the Fermi level rises. When ΔH_2 is dominant over V_{Cd}, the Fermi level is pinned by the host electronic states ΔH_1 and ΔH_2; in this case, the Fermi level reaches its highest. With the increase of μ_{Cd} along line A-B, the formation energy of As_{Te} decreases [Fig. 3(a)]. When the acceptor $As_{Te}(-)$ is dominant over ΔH_2, the Fermi level begins to decrease. At the chemical potential of point B, the Fermi level reaches a minimum because the formation energy of As_{Te} is the lowest at this point. Note that the formation energy of V_{Te} decreases as μ_{Cd} increases [Fig. 3(a)]. From Fig. 5(c), we find that V_{Te} and As_{Te} are of the same order of magnitude at point B, indicating that V_{Te} and ΔH_1 collectively compensate the acceptor As_{Te}, which confirms our predictions in Fig. 3(e). Along line B-C, the formation energy of As_{Te} increases, while the formation energy of V_{Te} continues to decrease [Fig. 3(a)]; consequently,

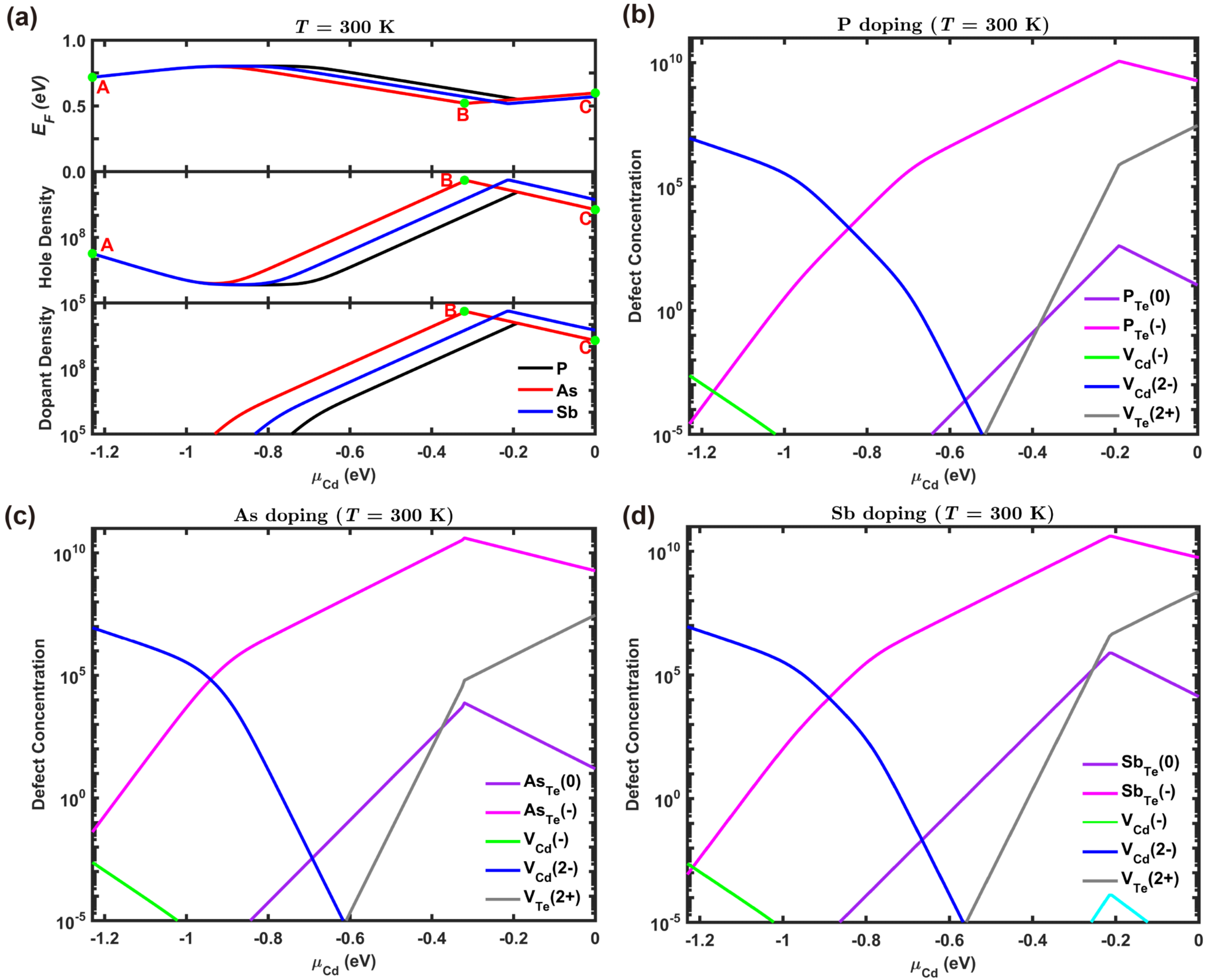

FIG. 4. Simulated results for group-V (P, As, and Sb) doped CdTe at $T = 300$ K. (a) Fermi level (E_F), hole density, dopant density, and (b)–(d) defect concentration, as functions of μ_{Cd}. Hole density, dopant density, and defect concentration are given in cm^{-3}.

the Fermi level is pushed up. In Fig. 5(a), the hole density shows an inverse trend with respect to the Fermi level, which results from the fact that the hole density is proportional to $\exp(-E_F)$ [Eq. (6)]. The As dopant density follows the same trend as $\mathrm{As_{Te}}(-)$ since the negatively charged $\mathrm{As_{Te}}(-)$ is dominant among the total As dopants. The formation energy of $\mathrm{As_{Te}}(-)$ varies with different rates because it depends on both the formation energy of $\mathrm{As_{Te}}(0)$ in Fig. 3(a) and the Fermi level E_F in Fig. 5(a), which can be understood from Eq. (3). From Figs. 5(b)–5(d), we find that the *AX* centers for all group-V dopants exhibit rather low concentrations, and thus cannot be a limiting factor for *p*-type doped CdTe. Table I summarizes the simulated results at the chemical potential of point *B*, where the hole densities achieve the highest. From Table I, we can see that all group-V dopants can achieve a hole density of $\sim 10^{17}\mathrm{cm}^{-3}$ when the growth temperature is at 850 K, corresponding to the Fermi level around 0.45 eV above the VBM.

Quenching is an effective method to reduce the Fermi level and enhance the hole density. Figure 6 shows our simulation after quenching from 850 to 300 K. We can see that the Fermi levels are reduced to 0.13–0.25 eV while maintaining relatively high hole densities at $10^{15}-10^{17}\mathrm{cm}^{-3}$ after quenching, as listed in Table I. In contrast, at the equilibrium growth temperature of $T = 300$ K shown in Fig. 4, the Fermi levels are pinned above 0.5 eV, and hole densities are limited to $\sim 10^{10}\mathrm{cm}^{-3}$. Therefore, it is necessary to grow at high temperatures and then quench to room temperature to obtain the high hole density and the low Fermi level. Note that, during the quenching process, the concentrations of defects with different charge states in the same configuration are redistributed according to their weights at $T = 300$ K, while maintaining the total defect concentration at growth temperature $T = 850$ K. For example, $\mathrm{As_{Te}}(0)$ and $\mathrm{As_{Te}}(-)$ are both in T_d symmetry. After redistributing, the concentration of $\mathrm{As_{Te}}(-)$ will be lowered, because defect ionization becomes more challenging at $T = 300$ K. This situation is particularly severe for $\mathrm{Sb_{Te}}$ due to its deep ionization energy. As shown in Fig. 6(d), the concentration of $\mathrm{Sb_{Te}}(-)$ is lower than that of $\mathrm{Sb_{Te}}(0)$ under the chemical-potential growth conditions of

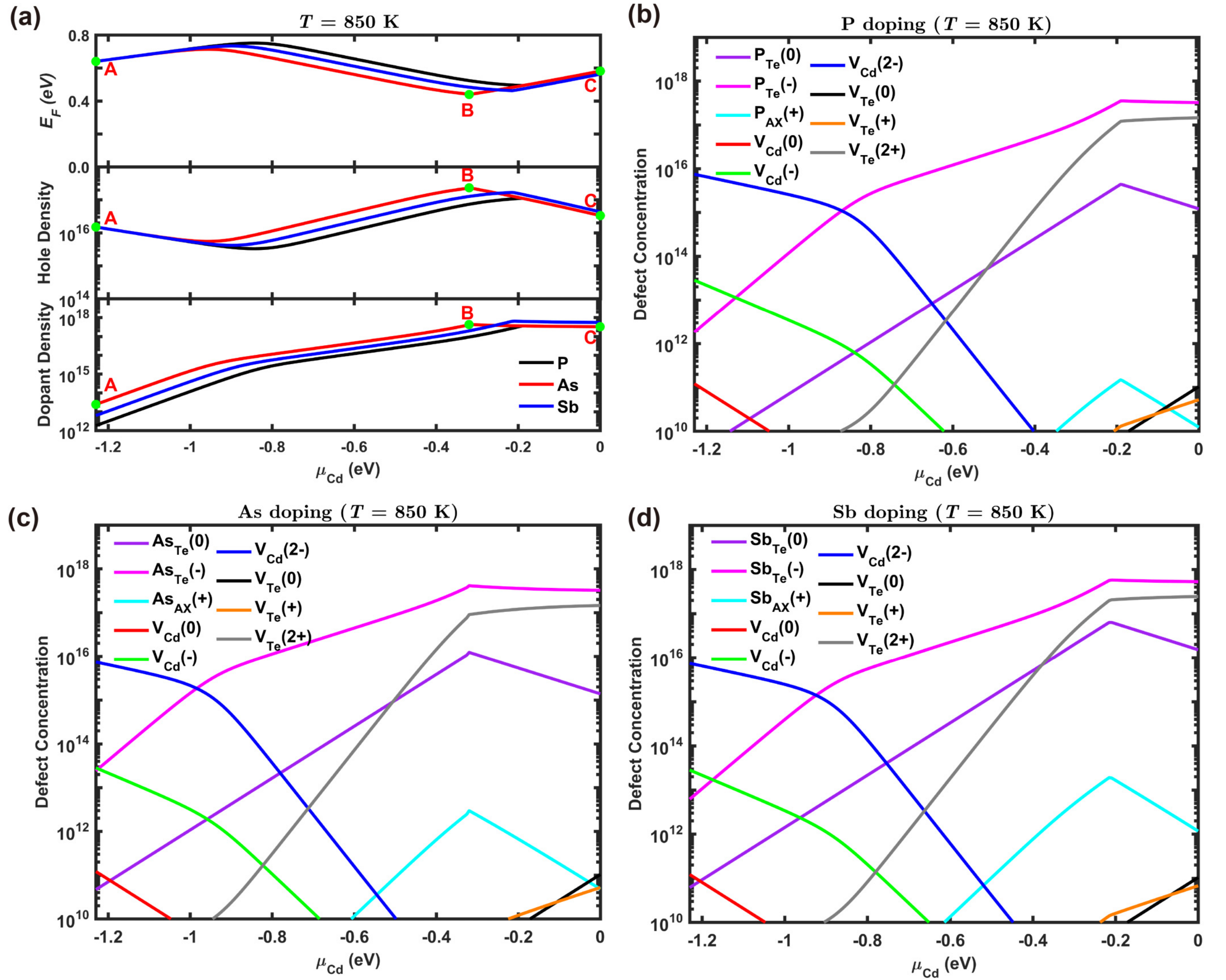

FIG. 5. Simulated results for group-V (P, As, and Sb) doped CdTe at $T = 850$ K. (a) Fermi level (E_F), hole density, dopant density, and (b)–(d) defect concentration, as functions of μ_{Cd}. Hole density, dopant density, and defect concentration are given in cm^{-3}.

Cd-poor/Te-poor/Sb-rich. As a result, Sb doping exhibits the poorest performance among group-V dopants, characterized by the lowest hole density. In contrast, As doping shows the most favorable behavior, achieving the highest hole density of $1.1 \times 10^{17} cm^{-3}$. This can be attributed to its relatively low combined formation energy and shallow acceptor level, allowing for more dopants to be introduced and subsequently ionized. Our results are consistent with previous experimental

TABLE I. Minimum Fermi levels (E_F), maximum hole densities, and dopant densities for group-V (P, As, and Sb) doping at $T = 300$ K, $T = 850$ K, and quenched from 850 to 300 K.

		E_F (eV)	Hole (cm^{-3})	Dopant (cm^{-3})
$T = 300$ K	P_{Te}	0.55	1.1×10^{10}	1.1×10^{10}
	As_{Te}	0.52	4.0×10^{10}	4.0×10^{10}
	Sb_{Te}	0.52	4.0×10^{10}	4.0×10^{10}
$T = 850$ K	P_{Te}	0.49	1.1×10^{17}	3.6×10^{17}
	As_{Te}	0.44	2.3×10^{17}	4.2×10^{17}
	Sb_{Te}	0.46	1.7×10^{17}	6.3×10^{17}
Quenched from 850 to 300 K	P_{Te}	0.15	6.0×10^{16}	3.6×10^{17}
	As_{Te}	0.13	1.1×10^{17}	4.2×10^{17}
	Sb_{Te}	0.25	1.2×10^{15}	6.3×10^{17}

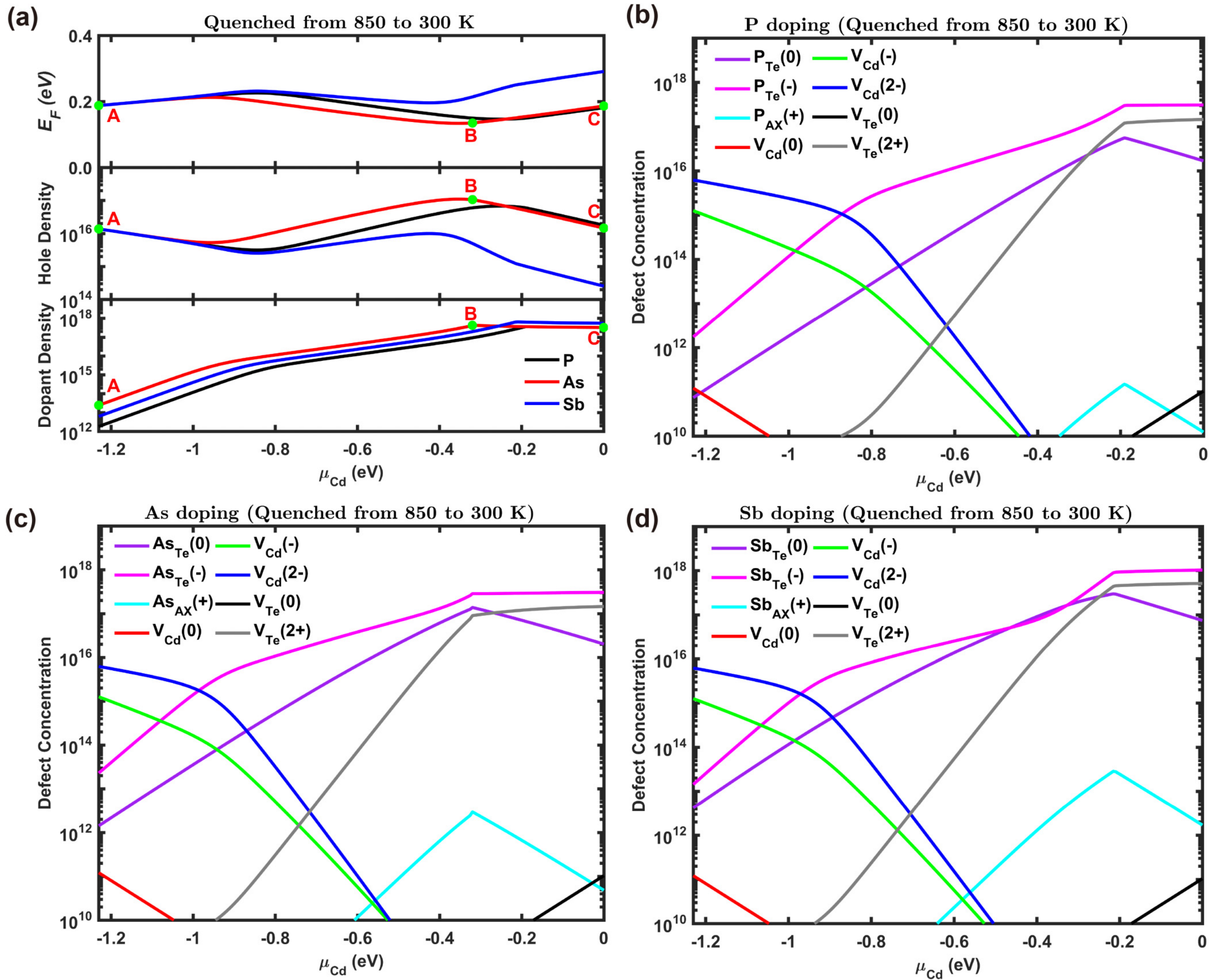

FIG. 6. Simulated results for group-V (P, As, and Sb) doped CdTe when quenching from 850 to 300 K. (a) Fermi level (E_F), hole density, dopant density, and (b)–(d) defect concentration, as functions of μ_{Cd}. Hole density, dopant density, and defect concentration are given in cm^{-3}.

results [11–13,53,54], which obtain the hole density in a range of $10^{15}-10^{17} cm^{-3}$.

IV. CONCLUSIONS

In conclusion, our systematic first-principles calculations including spin-orbital coupling show that P, As, and Sb all can achieve hole densities within the range of $10^{15}-10^{17} cm^{-3}$. We show that *AX* centers are unstable and thus cannot limit the *p*-type doping. Notably, the observed limit in hole density arises from the self-compensation mechanisms originating from the native vacancies and band-edge excitations. Our results, utilizing detailed balance equations, also highlight As (arsenic) as the most effective dopant among group-V dopants, due to its low combined formation energy and ionization energy level. This study unravels the origin of the hole density pinning in group-V doped CdTe and more importantly, it emphasizes the importance of the band-edge excitations in limiting the dopability of semiconductors.

ACKNOWLEDGMENTS

This work is supported by the National Natural Science Foundation of China (Grants No. 12088101, No. 11991060, No. 12204471, and No. U2230402). We also acknowledge computational support from the Beijing Computational Science Research Center (CSRC).

[1] C. H. Henry, Limiting efficiencies of ideal single and multiple energy gap terrestrial solar cells, J. Appl. Phys. **51**, 4494 (1980).

[2] J. J. Loferski, Theoretical considerations governing the choice of the optimum semiconductor for photovoltaic solar energy conversion, J. Appl. Phys. **27**, 777 (1956).

[3] W. Shockley and H. J. Queisser, Detailed balance limit of efficiency of $p-n$ junction solar cells, J. Appl. Phys. **32**, 510 (1961).

[4] Best research-cell efficiency chart, National Renewable Energy Laboratory, https://www.nrel.gov/pv/cell-efficiency.html (accessed February, 2024).

[5] M. A. Green, K. Emery, Y. Hishikawa, W. Warta, and E. D. Dunlop, Solar cell efficiency tables (version 46), Prog. Photovoltaics: Res. Appl. **23**, 805 (2015).

[6] J.-H. Yang, W.-J. Yin, J.-S. Park, J. Ma, and S.-H. Wei, Review on first-principles study of defect properties of CdTe as a solar cell absorber, Semicond. Sci. Technol. **31**, 083002 (2016).

[7] J. Ma, D. Kuciauskas, D. Albin, R. Bhattacharya, M. Reese, T. Barnes, J. V. Li, T. Gessert, and S.-H. Wei, Dependence of the minority-carrier lifetime on the stoichiometry of CdTe using time-resolved photoluminescence and first-principles calculations, Phy. Rev. Lett. **111**, 067402 (2013).

[8] J.-H. Yang, L. Shi, L.-W. Wang, and S.-H. Wei, Non-radiative carrier recombination enhanced by two-level process: A first-principles study, Sci. Rep. **6**, 21712 (2016).

[9] S.-H. Wei and S. B. Zhang, Chemical trends of defect formation and doping limit in II-VI semiconductors: The case of CdTe, Phys. Rev. B **66**, 155211 (2002).

[10] J. Perrenoud, L. Kranz, C. Gretener, F. Pianezzi, S. Nishiwaki, S. Buecheler, and A. N. Tiwari, A comprehensive picture of Cu doping in CdTe solar cells, J. Appl. Phys. **114**, 174505 (2013).

[11] A. Nagaoka, K. Nishioka, K. Yoshino, R. Katsube, Y. Nose, T. Masuda, and M. A. Scarpulla, Comparison of Sb, As, and P doping in Cd-rich CdTe single crystals: Doping properties, persistent photoconductivity, and long-term stability, Appl. Phys. Lett. **116**, 132102 (2020).

[12] G. Kartopu, O. Oklobia, D. Turkay, D. R. Diercks, B. P. Gorman, V. Barrioz, S. Campbell, J. D. Major, M. K. Al Turkestani, S. Yerci *et al.*, Study of thin film poly-crystalline CdTe solar cells presenting high acceptor concentrations achieved by *in-situ* arsenic doping, Sol. Energy Mater. Sol. Cells **194**, 259 (2019).

[13] B. E. McCandless, W. A. Buchanan, C. P. Thompson, G. Sriramagiri, R. J. Lovelett, J. Duenow, D. Albin, S. Jensen, E. Colegrove, J. Moseley *et al.*, Overcoming carrier concentration limits in polycrystalline CdTe thin films with *in situ* doping, Sci. Rep. **8**, 14519 (2018).

[14] M. Zandian, A. C. Chen, D. D. Edwall, J. G. Pasko, and J. M. Arias, p-type arsenic doping of $Hg_{1-x}Cd_xTe$ by molecular beam epitaxy, Appl. Phys. Lett. **71**, 2815 (1997).

[15] E. Colegrove, J. H. Yang, S. P. Harvey, M. R. Young, J. M. Burst, J. N. Duenow, D. S. Albin, S. H. Wei, and W. K. Metzger, Experimental and theoretical comparison of Sb, As, and P diffusion mechanisms and doping in CdTe, J. Phys. D: Appl. Phys. **51**, 075102 (2018).

[16] D. J. Chadi, Predictor of p-type doping in II-VI semiconductors, Phys. Rev. B **59**, 15181 (1999).

[17] C. H. Park and D. J. Chadi, Bulk lattice instability in II-VI semiconductors and its effect on impurity compensation, Phys. Rev. Lett. **75**, 1134 (1995).

[18] J. H. Yang, W. J. Yin, J. S. Park, J. Burst, W. K. Metzger, T. Gessert, T. Barnes, and S.-H. Wei, Enhanced p-type dopability of P and As in CdTe using non-equilibrium thermal processing, J. Appl. Phys. **118**, 025102 (2015).

[19] M.-H. Du, Density functional calculations of native defects in $CH_3NH_3PbI_3$: Effects of spin–orbit coupling and self-interaction error, J. Phys. Chem. Lett. **6**, 1461 (2015).

[20] D. West, Y. Y. Sun, H. Wang, J. Bang, and S. B. Zhang, Native defects in second-generation topological insulators: Effect of spin-orbit interaction on Bi_2Se_3, Phys. Rev. B **86**, 121201(R) (2012).

[21] Z. G. Yu and Y.-W. Zhang, Effect of spin-orbit coupling on formation of native defects in Weyl fermion semimetals: The case of TX (T = Ta, Nb; X = As, P), Phys. Rev. B **94**, 195206 (2016).

[22] W.-F. Li, C. Fang, and M. A. van Huis, Strong spin-orbit splitting and magnetism of point defect states in monolayer WS_2, Phys. Rev. B **94**, 195425 (2016).

[23] A. Goyal, P. Gorai, E. S. Toberer, and V. Stevanović, First-principles calculation of intrinsic defect chemistry and self-doping in PbTe, npj Comput. Mater. **3**, 42 (2017).

[24] J. Pan, W. K. Metzger, and S. Lany, Spin-orbit coupling effects on predicting defect properties with hybrid functionals: A case study in CdTe, Phys. Rev. B **98**, 054108 (2018).

[25] I. Chatratin, B. Dou, S.-H. Wei, and A. Janotti, Doping limits of phosphorus, arsenic, and antimony in CdTe, J. Phys. Chem. Lett. **14**, 273 (2023).

[26] G. Kresse and D. Joubert, From ultrasoft pseudopotentials to the projector augmented-wave method, Phys. Rev. B **59**, 1758 (1999).

[27] G. Kresse and J. Furthmüller, Efficient iterative schemes for *ab initio* total-energy calculations using a plane-wave basis set, Phys. Rev. B **54**, 11169 (1996).

[28] J. Paier, M. Marsman, K. Hummer, G. Kresse, I. C. Gerber, and J. G. Ángyán, Screened hybrid density functionals applied to solids, J. Chem. Phys. **124**, 154709 (2006).

[29] S. Steiner, S. Khmelevskyi, M. Marsmann, and G. Kresse, Calculation of the magnetic anisotropy with projected-augmented-wave methodology and the case study of disordered $Fe_{1-x}Co_x$ alloys, Phys. Rev. B **93**, 224425 (2016).

[30] G. Lutz, *Semiconductor Radiation Detectors. Device Physics* (Springer, Berlin, 1999).

[31] S.-H. Wei, Overcoming the doping bottleneck in semiconductors, Comput. Mater. Sci. **30**, 337 (2004).

[32] J. Ma, S.-H. Wei, T. A. Gessert, and K. K. Chin, Carrier density and compensation in semiconductors with multiple dopants and multiple transition energy levels: Case of Cu impurities in CdTe, Phys. Rev. B **83**, 245207 (2011).

[33] M. A. Green, Intrinsic concentration, effective densities of states, and effective mass in silicon, J. Appl. Phys. **67**, 2944 (1990).

[34] R. Romestain and C. Weisbuch, Optical detection of cyclotron resonance in semiconductors, Phys. Rev. Lett. **45**, 2067 (1980).

[35] K. Kim, W. R. L. Lambrecht, B. Segall, and M. van Schilfgaarde, Effective masses and valence-band splittings in GaN and AlN, Phys. Rev. B **56**, 7363 (1997).

[36] S. Z. Karazhanov and L. C. Lew Yan Voon, *Ab initio* studies of the band parameters of III–V and II–VI zinc-blende semiconductors, Semiconductors **39**, 161 (2005).

[37] D. Krasikov, A. Knizhnik, B. Potapkin, and T. Sommerer, Why shallow defect levels alone do not cause high resistivity in CdTe, Semicond. Sci. Technol. **28**, 125019 (2013).

[38] K. Yamaguchi, K. Hongo, K. Hack, I. Hurtado, and D. Neuschütz, Measurement and assessment of the thermodynamic

properties and the phase diagram of the Cd-Te System, Mater. Trans., JIM **41**, 790 (2000).
[39] B. Dou, Q. Sun, and S.-H. Wei, Optimization of doping CdTe with group-V elements: A first-principles study, Phys. Rev. Appl. **15**, 054045 (2021).
[40] J.-H. Yang, W.-J. Yin, J.-S. Park, and S.-H. Wei, Self-regulation of charged defect compensation and formation energy pinning in semiconductors, Sci. Rep. **5**, 16977 (2015).
[41] E. Molva, J. L. Pautrat, K. Saminadayar, G. Milchberg, and N. Magnea, Acceptor states in CdTe and comparison with ZnTe. General trends, Phys. Rev. B **30**, 3344 (1984).
[42] F. A. Selim and F. A. Kröger, The defect structure of phosphorus-doped CdTe, J. Electrochem. Soc. **124**, 401 (1977).
[43] C. Kraft, A. Brömel, S. Schönherr, M. Hädrich, U. Reislöhner, P. Schley, G. Gobsch, R. Goldhahn, W. Wesch, and H. Metzner, Phosphorus implanted cadmium telluride solar cells, Thin Solid Films **519**, 7153 (2011).
[44] J. Gu, T. Kitahara, K. Kawakami, and T. Sakaguchi, Ohmic contact and impurity conduction in P−doped CdTe, J. Appl. Phys. **46**, 1184 (2008).
[45] Y. Proskuryakov, K. Durose, J. Major, M. Al Turkestani, V. Barrioz, S. Irvine, and E. Jones, Doping levels, trap density of states and the performance of co-doped CdTe (As, Cl) photovoltaic devices, Sol. Energy Mater. Sol. Cells **93**, 1572 (2009).
[46] T. Ablekim, S. K. Swain, W.-J. Yin, K. Zaunbrecher, J. Burst, T. M. Barnes, D. Kuciauskas, S.-H. Wei, and K. G. Lynn, Self-compensation in arsenic doping of CdTe, Sci. Rep. **7**, 4563 (2017).
[47] J. M. Arias, S. H. Shin, D. E. Cooper, M. Zandian, J. G. Pasko, E. R. Gertner, R. E. DeWames, and J. Singh, *p*-type arsenic doping of CdTe and HgTe/CdTe superlattices grown by photoassisted and conventional molecular-beam epitaxy, J. Vac. Sci. Technol., A **8**, 1025 (1990).
[48] E. Colegrove, S. P. Harvey, J. H. Yang, J. M. Burst, J. N. Duenow, D. S. Albin, S. H. Wei, and W. K. Metzger, Antimony diffusion in CdTe, IEEE J. Photovoltaics **7**, 870 (2017).
[49] M.-H. Du, H. Takenaka, and D. J. Singh, Carrier compensation in semi-insulating CdTe: First-principles calculations, Phys. Rev. B **77**, 094122 (2008).
[50] K. G. Biswas and M. H. Du, What causes high resistivity in CdTe, New J. Phys. **14**, 063020 (2012).
[51] V. Lordi, Point defects in Cd(Zn)Te and TlBr: Theory, J. Cryst. Growth **379**, 84 (2013).
[52] S. Lany, V. Ostheimer, H. Wolf, and T. Wichert, Vacancies in CdTe: Experiment and theory, Phys. B (Amsterdam) **308**, 958 (2001).
[53] J. M. Burst, J. N. Duenow, D. S. Albin, E. Colegrove, M. O. Reese, J. A. Aguiar, C. S. Jiang, M. K. Patel, M. M. Al-Jassim, D. Kuciauskas *et al.*, CdTe solar cells with open-circuit voltage breaking the 1 V barrier, Nat. Energy **1**, 16015 (2016).
[54] J. M. Burst, S. B. Farrell, D. S. Albin, E. Colegrove, M. O. Reese, J. N. Duenow, D. Kuciauskas, and W. K. Metzger, Carrier density and lifetime for different dopants in single-crystal and polycrystalline CdTe, APL Mater. **4**, 116102 (2016).